Applied Surface Science 526 (2020) 146626

Contents lists available at ScienceDirect

Applied Surface Science

journal homepage: www.elsevier.com/locate/apsusc

Polyaniline engineering defect-induced nitrogen doped carbon-supported Co_3O_4 hybrid composite as a high-efficiency electrocatalyst for oxygen evolution reaction

Xiaodong Chen[a,b,e,1], Ya Chen[d,1], Xiang Luo[a,b,1], Hele Guo[c], Nannan Wang[a], Dawei Su[b], Chao Zhang[c,*], Tianxi Liu[c], Guoxiu Wang[b,*], Lifeng Cui[a,*]

[a] School of Materials Science and Engineering, Dongguan University of Technology, Dongguan, Guangdong 523808, PR China
[b] Center for Clean Energy Technology, School of Mathematical and Physical Science, Faculty of Science, University of Technology Sydney, NSW 2007, Australia
[c] State Key Laboratory for Modification of Chemical Fibers and Polymer Materials, College of Materials Science and Engineering, Innovation Center for Textile Science and Technology, Donghua University, Shanghai 201620, PR China
[d] School of Physical Science and Technology, ShanghaiTech University, Shanghai 201210, PR China
[e] Department of Applied Chemistry, School of Science, Xi'an Jiaotong University, Xi'an 710049, PR China

ARTICLE INFO

Keywords:
OER
Co_3O_4/CN HNPs
Crystal defect sites
Oxygen-vacancy sites
Strong interactions

ABSTRACT

The development of earth-abundance electrocatalyst with high performance for oxygen evolution reaction (OER) is of paramount importance in sustainable water splitting. Herein, the novel defect-induced nitrogen-doped carbon-supported Co_3O_4 nanoparticles is successfully fabricated as OER electrocatalyst (denoted as Co_3O_4/CN HNPs) through a wetness-impregnation treatment of Co/polyaniline (PANI) followed by a thermal annealing. This advanced architecture of Co_3O_4/CN HNPs can not only improve its conductivity and electrocatalytically active sites but also generate a large number of oxygen-vacancy defects and crystal defects, which effectively exert the preponderance in facilitating interfacial electronic transfer and optimizing the adsorption energy for intermediates, thus imparting the extraordinary activities in catalyzing OER. In addition, there are evidences demonstrating the formation of C-N coordination bonds through the strong interaction of the interconnected interface and the generation of pyridinic-N species after the annealing treatment, which enables the structural stability to get further strengthened and accelerates oxygen releasing for reduction of OER overpotential, respectively. Benefiting from the above desirable properties, the Co_3O_4/CN HNPs affords a lower overpotential of 290 mV at a current density of 10 mA cm^{-2} as compared to those of pure Co_3O_4 and PANI, outperforming commercial IrO_2 and the representative Co_3O_4-based OER electrocatalysts as recently reported. Moreover, the Co_3O_4/CN HNPs also exhibits long durability with negligible activity degeneration at a current density of 10 mA cm^{-2} for 20 h.-.

1. Introduction

The existent contradiction between dwindling fossil fuels and increasing energy demands pushes forward the extensive research in the field of water electrolysis system due to its merits of the low expenditure and the environmental friendliness [1–3]. Electrochemical OER is investigated as the rate-determining step on account of the sluggish kinetics in the whole process of water splitting, in which the exploitment of art-of-the-state electrocatalyst is of great importance for addressing above-mentioned issues [4–6]. To date, noble-metal-based materials, such as the iridium dioxides (IrO_2) and ruthenium dioxides (RuO_2) are well-known for their high-performance OER activities, nevertheless, the non-negligible drawbacks of high cost and scarcity have restricted their commercial-scale application [7–9]. Therefore, it is highly desirable to search an accessible electrocatalyst as alternative to achievement of sustainable OER. To date, persistent efforts have devoted to the investigation of the transition-metal oxides, hydroxides, selenides, sulfides, nitrides, phosphides, and so on [10–13]. Among them, the transition-metal oxide Co_3O_4 is preferentially elected as the most promising candidate for OER due to its advantages of high abundance, structure diversity and durability under alkaline conditions [14,15].

* Corresponding authors.
E-mail addresses: czhang@dhu.edu.cn (C. Zhang), Guoxiu.Wang@uts.edu.au (G. Wang), lcui@dgut.edu.cn (L. Cui).
[1] These authors contributed equally to this work.

https://doi.org/10.1016/j.apsusc.2020.146626
Received 26 February 2020; Received in revised form 20 April 2020; Accepted 7 May 2020
Available online 11 May 2020
0169-4332/

In reality, the considerable researches have put great efforts into the development of Co_3O_4-based catalysts with high surface areas, increased electrical conductivities and unique facet structures, nevertheless, the corresponding OER activities are not desirable as expected and still need to be further promoted [16–26]. Recently, both experimental and computational studies have demonstrated that the introduction of zero-dimensional point defects (oxygen vacancies) and two-dimensional planar defects (crystal defects) into the transition-metal oxides can provide the functionalities to modulate the electronic structure, enhance the electrical conductivity and optimize the adsorption energy of reactants and intermediates, thus accelerating electrochemical reactions kinetics [27–29]. For instance, Yin *et al.* [30] synthesize $CoFe_2O_4$ nanosheets with the enriched oxygen defects for overall water splitting, and demonstrate that alone with oxygen defects doping, the density of states across the Fermi level increases as well, which can be conductive to the fast electron transportation. Hu *et al.* [31] construct the ultrathin defect-enriched 3D Se-$(NiCo)S_x/(OH)_x$ nanosheets for overall water splitting, which are more favorable for the adsorption of H_2O and OH^-, hence improving the OER and HER activities, respectively. Fan *et al.* [32] fabricate the 3D iron fluoride-oxide nanoporous films with abundant scattered defects, including interphase boundaries, stacking faults, oxygen vacancies, and dislocations on the surfaces/interface, which expose the additional reaction sites and lower the adsorption energy of the reactant and product in OER and HER. These results conclude that the existing abundant defects can exert the Co_3O_4-based catalysts with suitable chemical properties, electronic structure and additional electrocatalytically active sites, which can be considered to be an effective strategy for further enhancing OER activities [33,34].

Herein, a pioneering method is demonstrated to accomplish the task of engineering abundant defects into Co_3O_4 surface to expose the additional active sites. In this contribution, polyaniline (PANI) is preferentially selected as the self-sacrificing template due to its unique π-conjugated structures and affluent nitrogen species with lone electron pairs, which can afford enough coordination sties to anchor Co ions and thus generate Co/PANI as precursor [35–38]. Then, the corresponding defects enriched Co_3O_4/CN HNPs can be successfully synthesized after an annealing treatment. More concretely, the formation of coupled carbon materials in this electrocatalyst not only increases the conductivity but also can be rendered as substrate for dispersing and fabricating three-dimensional structure of Co_3O_4 nanoparticles with abundant exposed active sites, on which the permeation and the adherence of electrolyte as well as the detachment of oxygen are becoming extremely feasible. In addition, the generation of Co—N coordination bonds and existence of pyridinic-N species over the Co_3O_4/CN HNPs are instrumental in strengthening structural stability and reducing OER overpotential, respectively. More importantly, there are abundant oxygen-vacancy defects and crystal defects existing on the surface of the Co_3O_4 nanoparticles, which are favorable for significantly accelerating internal electronic transfer and optimizing the adsorption energy for intermediates. Aa a consequence, the Co_3O_4/CN HNPs delivers a low overpotential of 290 mV at a current density of 10 mA cm^{-2} and a small Tafel slope of 59 mV dec^{-1} in 1 M KOH electrolyte, superior than those of pure Co_3O_4, PANI, and commercial IrO_2, which also outperforms the representative Co_3O_4-based OER electrocatalysts in Table S1. In addition, the Co_3O_4/CN HNPs exhibits unprecedented stability with negligible activity degeneration at a current density of 10 mA cm^{-2} for 20 h.

2. Experimental

2.1. Chemicals

Cobalt acetate tetrahydrate ($Co(OAc)_2{\cdot}4H_2O$, 99.5%), Hydrochloric acid (HCl, 36.5%), Ammonium persulphate ($(NH_4)_2S_2O_8$, A.R.), Aniline (99.5%) and Ethanol (99.5%) are obtained from Sinopharm Chemicals. Potassium hydroxide (KOH, 90%) is purchased from Sigma Aldrich. Deionized (DI) water is utilized throughout the experiments.

2.2. Chemical synthesis of the PANI, the Co_3O_4/CN HNPs and the Co_3O_4

2.2.1. Preparation of the PANI

Polyamine (PANI) is prepared on the process that 1.62 g ammonium persulfate is dissolved in 5.0 mL deionized water (solution A), and 0.92 mL purified aniline is dissolved in 5.0 mL 2.0 M HCl (solution B). Solution A is poured quickly into solution B until the stirred mixture is discolored. Then, the mixture is placed in the cold bath with the temperature of 0 °C for 24 h. After purged with deionized water and ethanol, the targeted PANI is acquired.

2.2.2. Preparation of the Co_3O_4/CN HNPs

The Co_3O_4/CN HNPs is fabricated by combination of both a wetness-impregnation method and subsequent annealing route. In a typical preparation of the Co_3O_4/CN HNPs, the required amount of 170 mg Co $(OAc)_2{\cdot}4H_2O$ is diluted to 50 mL with deionized water and then 200 mg as-obtained PANI is also added which is stirred at 50 °C until all the water is evaporated. The resultant precipitate (Co/PANI) is dried at 70 °C in air for 12 h and followed by the annealing treatment in the muffle oven at 300 °C for 4 h with temperature heating rate of 5 °C min^{-1}.

2.2.3. Preparation of the Co_3O_4

The weighted 170 mg $Co(OAc)_2{\cdot}4H_2O$ is firstly dried in the muffle oven at 70 °C for 4 h. Subsequently, the sample is calcined in the muffle oven at 300 °C for 4 h with temperature heating rate of 5 °C min^{-1}.

2.3. Characterization

The morphology of power samples is examined by field-emissions scanning electron microscopy (FESEM, Ultra 55) and transmission electron microscopy (TEM, Tecnai G2 20 TWIN). X-ray diffraction (XRD) patterns are performed from $2\theta = 10°{\sim}90°$ by using an X' Pert Pro X-ray diffractometer equipped with a Cu K_α radiation ($\lambda = 0.1542$ nm) at a current of 40 mA and a voltage of 40 kV, respectively. The chemical composition of the samples is determined by inductively coupled plasma-atomic emission spectrometry (ICP-AES). Fourier transform infrared (FTIR) spectra of power samples are measured by Nicolet Nexus-670 (Nicolet, USA) in the range of 400–4000 cm^{-1}. Raman spectra are collected using a Lab RAM-HR Confocal Laser Micro Raman Spectrometer with a 532 nm laser diode as the excitation source. The chemical state of samples are detected by X-ray photoelectron spectroscopy (XPS) analyses with VG ESCALAB 220I-XL instrument. All the XPS spectra are corrected according to C 1s line at 284.8 eV. Curve fitting and background subtraction are accomplished using Casa XPS software.

2.4. Electrochemical characterization

Electrocatalytic measurements: The electrochemical activities of all samples for the OER are examined with CHI 660D electrochemical workstation in a standard three electrode system using the Ag/AgCl electrode, graphite rod and the catalyst loaded rotating disk electrode as the reference electrode, counter electrode and working electrode, respectively. The catalyst ink is prepared by dispersing 5 mg of samples into 350 μL of ethanol and 95 μL of Nafion solution (5 wt%). Upon sonication, 5 μL of the catalyst ink is deposited onto 5 mm diameter polished glassy carbon electrode (Gamry Instruments, Inc.) with a mass loading of ~0.295 mg cm^{-2} and dried at room temperature. Linear sweep voltammetry (LSV) is carried out for the polarization curves with a sweep rate of 5 mV s^{-1} in 1 M KOH. The electrochemical impedance spectroscopy (EIS) measurements are conducted at 1.52 V vs. RHE over a frequency range 0.01–10^5 Hz. The double-layer capacitances (Cdl) are

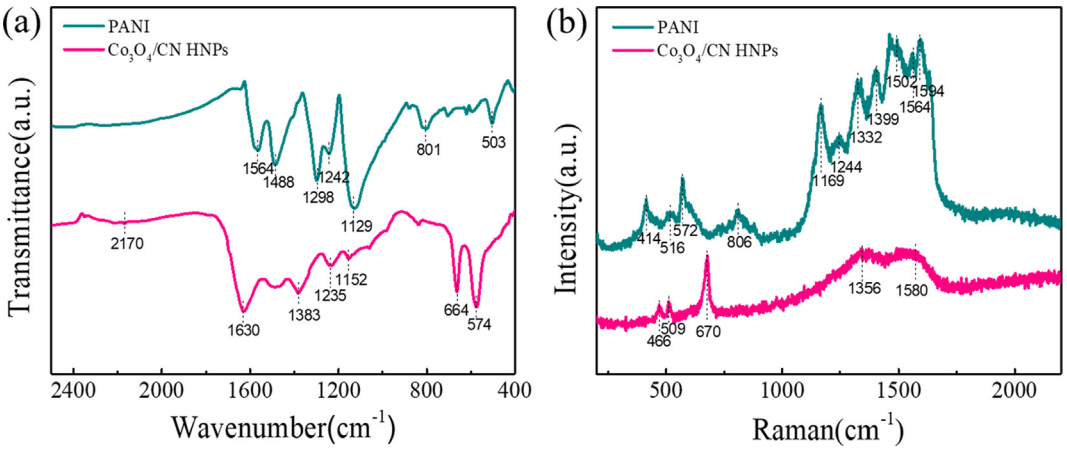

Fig. 1. (a) FTIR spectrum of PANI and Co_3O_4/CN HNPs. (b) Raman spectrum of PANI and Co_3O_4/CN HNPs.

estimated by cyclic votammetry (CV) in the region of 1.20–1.35 V vs. RHE at various scan rates of 20, 40, 60, 80 and 100 mV s^{-1}, respectively. By plotting the j (j = ja − jc) at the potential of 1.26 V vs. RHE against the scan rate, the linear slope C_{dl} is used to evaluate the electrochemical surface area (ECSA).

3. Results and discussion

The Co_3O_4/CN HNPs can be synthesized by combination of wetness-impregnation method and thermal annealing treatment. Briefly stated, the polyaniline (PANI) is firstly prepared though the polymerization of aniline in acidic environment [39]. Subsequently, though Co−N coordination, the Co^{2+} ions from $Co(OAc)_2{\cdot}4H_2O$ can be availably anchored over the PANI to generate the Co/PANI precursor [38,40]. Eventually, the as-fabricated Co/PANI precursor can be availably converting into the desirable Co_3O_4/CN HNPs after an annealing treatment. The FTIR spectra is acquired to recognize the chemical structure of PANI and Co_3O_4/CN HNPs, as illustrated in Fig. 1a. Several prominent characteristic absorption peaks of PANI are observed at 1564 cm^{-1} (stretching vibration of C=C and C=N in quinoid rings), 1488 cm^{-1} (stretching mode of C=C in benzenoid rings), 1298 cm^{-1} (C−N stretching mode of benzenoid rings), 1242 cm^{-1} (C−N^+ stretching vibration), 1129 cm^{-1} (in-plane bending of C−H in quinoid rings), 801 cm^{-1} (C−H deformation vibrations in the para-substituted ring) and 503 cm^{-1} (hydrogen chlorine counter ions), revealing the accomplished preparation of PANI under our condition [41–43]. Referring to Co_3O_4/CN HNPs, there are no complete characteristic peaks corresponding to PANI, proving that when the Co/PANI precursor undergoes an annealing treatment, its structure has been subjected to decomposition as expected. The characteristic peaks of Co_3O_4/CN HNPs at 1630 cm^{-1}, 1383 cm^{-1}, 1235 cm^{-1} and 1152 cm^{-1}, are assigned to the adsorbed H_2O molecules, the C−N stretching vibrations, the C−N^+ stretching vibrations and the vibrations of the −N^+= structure, respectively [42,44]. Besides this, the peaks located at 574 cm^{-1} and 664 cm^{-1} are attributed to the OB_3 (B represents Co^{3+} in an octahedral site) and the ABO (A represents the Co^{2+} in a tetrahedral site) vibrations in the spinel lattice of Co_3O_4 phase [45]. It's worth mentioning that there is a new weak characteristic peak appearing at 2170 cm^{-1}, suggesting the formation of Co−N coordination bond which is triggered by the strong interaction between C−N substrate and Co_3O_4 in the Co_3O_4/CN HNPs [46]. In this regard, the substitution of O atoms in the Co_3O_4 crystal lattice by N atoms corresponds to the decrease of Co valence state, which results from the fact that N affords a smaller electronegativity (3.04) than O (3.44) and thus there is less electron attraction from Co to N than the attraction from Co to O [47]. Correspondingly, the more oxygen vacancies can be generated during the N doping process to balance the decrease of Co valence state, which is favorable for enhancing the OER activities [48]. Besides, the high-stability property of Co−N coordinate bond is also mainly responsible for the long-term durability of Co_3O_4/CN HNPs at different OER stages [37]. Raman spectra is also examined to determine the chemical structure of PANI and Co_3O_4/CN HNPs as depicted in Fig. 1b. The Raman spectra of PANI exhibits several prominent characteristic peaks, such as 1594 cm^{-1} (the C−C stretching vibrations of the benzenoid ring), 1564 cm^{-1} (the C−C stretching vibrations of the benzenoid ring), 1502 cm^{-1} (the C−C stretching and N−H deformation vibration relative with the semiquinonoid structures), 1399 cm^{-1} (the C ∼ $N^{+\cdot}$ stretching vibrations of localized polaronic structures), 1332 cm^{-1} (the C−N stretching vibrations of more delocalized polarons), 1244 cm^{-1} (the benzene-ring deformation vibrations) and 1169 cm^{-1} (the C−H bending vibrations of the semi-quinonoid rings). Bands appeared at 806 cm^{-1}, 572 cm^{-1}, 516 cm^{-1} and 414 cm^{-1} are due to the protonation of PANI under acid synthesis conditions [42,43]. In contrast, there is a significantly change in the Raman spectra of Co_3O_4/CN HNPs. Thereinto, the remarkable peaks at 670 cm^{-1} (E_g), 509 cm^{-1} (E_{2g}) and 466 cm^{-1} (A_{1g}) are assigned to the Raman active modes of Co_3O_4 [44], whereas the noticeable Raman peaks at 1356 cm^{-1} and 1580 cm^{-1} are belonged to D band and G band, which represents the disordered and the graphitic phases, respectively [49,50], confirming a formation of microcrystalline graphite structure, which endows the Co_3O_4/CN HNPs with high electrical conductivity for OER.

The powder XRD patterns of the as-obtained PANI, Co_3O_4/CN HNPs, and Co_3O_4 are displayed in Fig. 2. As observed, the PANI presents diffraction peaks at 20.6° and 25.1°, which are indexed to the (1 0 0) plane of quinoid units about p-p stacking induced partial periodicity arrangement and (1 1 0) plane of benzenoid units [51]. In the contrast,

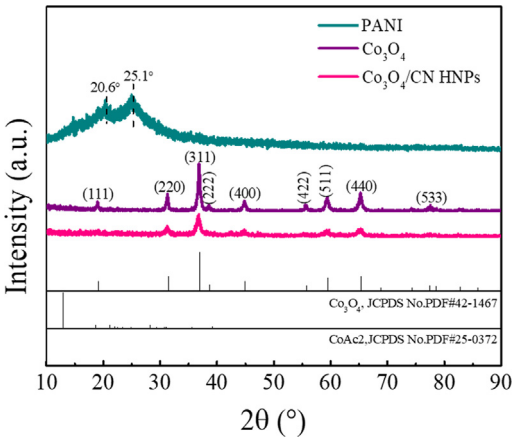

Fig. 2. XRD patterns of PANI, Co_3O_4 and Co_3O_4/CN HNPs.

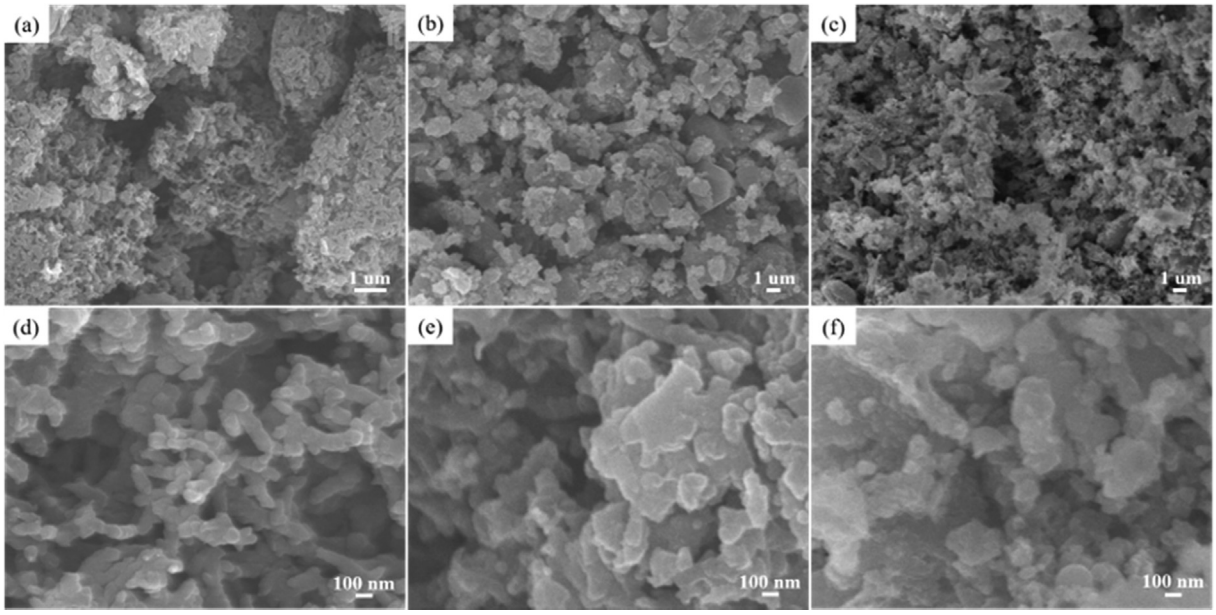

Fig. 3. SEM images of (a,d) PANI, (b,e) Co_3O_4/CN HNPs and (c, f) as-synthesized Co_3O_4.

there is no characteristic diffraction peaks of PANI that ascribe to Co_3O_4/CN HNPs, further indicating that its structure has been dissociated and carbonized in annealing process, which is in accordance with the FTIR and the Raman results. The prominent peaks of Co_3O_4/CN HNPs are located at 2θ values of 19.0°, 31.2°, 36.9°, 38.6°, 44.8°, 55.8°, 59.5°, 65.3° and 77.5° respectively where they are corresponded to the (1 1 1), (2 2 0), (3 1 1), (2 2 2), (4 0 0), (4 2 2), (5 1 1), (4 4 0) and (5 3 3) lattice planes of Co_3O_4 (JCPDS No. 42-1467) [47], which is consistent with XRD patterns of as-synthesized Co_3O_4. In addition to this, it is also found that the Co_3O_4/CN HNPs delivers the obvious weakening of Co_3O_4 characteristic diffraction peaks when compared with as-synthesized Co_3O_4, suggesting that the smaller Co_3O_4 nanoparticles are generated over the C—N substrate in the carbonized process of Co/PANI precursor [52], which are in favor of the increased exposed active sites for the Co_3O_4/CN HNPs.

The Field Emission Scanning Electron Microscopy (SEM) images and Transmission Electron Microscopy (TEM) images of PANI are exhibited in Fig. 3a, d, and Fig. S1a–c, revealing that its coral-like micro-morphology is comprised of the accumulation of ramous microrods with uniform diameters in the range 60–100 nm and lengths up to 200–500 nm (Fig. S2a, b). After loading of Co^{2+} ions, there are no significant variation in morphology as comparison with PANI (Fig. S3a, b), and there are also no Co^{2+} ions that are observed to aggregate to form distinguishable nanoparticles over the Co/PANI precursor (Fig. S4a, b). Meanwhile, High-angle annular dark-field scanning TEM (HAADF-STEM) image and corresponding EDX elemental mapping is executed to further probe the elemental composition and distribution of Co/PANI precursor as shown in Fig. S5a–d, the Co, N and C elements are examined to be coexisted in this precursor and the Co is homogeneously distributed rather than aggregated throughout the PANI support. In addition, the SEM images of Co_3O_4/CN HNPs as shown in Fig. 3b, e, elucidate that its surface morphology becomes rough and compacted after an annealing treatment. Moreover, there are also no discernible Co_3O_4 nanoparticles generated over C—N substrate as like the as-synthesized Co_3O_4, as depicted in Fig. 3c, f. Furthermore, the corresponding TEM images, high-resolution TEM (HRTEM) images and selected-area electron diffraction (SAED) of Co_3O_4/CN HNPs are displayed in Fig. 4a–g, respectively. More concretely, the lower-magnification TEM images in Fig. 4a, b clearly demonstrate that the ultrafine Co_3O_4 nanoparticles with the main size of 10–20 nm is well-dispersed and immobilized over the C—N substrate, allowing exposed multiple active sites for reactants and intermediates in the electrolyte [19,20]. In accordance with SAED results (Fig. 4c), the legible lattice interspacing of 4.68, 2.87, 2.35 and 2.04 Å obtained by HRTEM image (Fig. 4d) can be assigned to the (1 1 1), (2 2 0), (2 2 2) and (4 0 0) crystalline plane of Co_3O_4 phase but with a negligible lattice expansion. Remarkably, the well-resolved crystal defects caused by the lattice distortion and stacking faults are detected on the exposed facets (1 1 1) of Co_3O_4 crystalline (Fig. 4e). The existence of crystal defects is demonstrated to ameliorate the adsorption energy of intermediates for OER [53,29]. Furthermore, the HAADF-STEM image (Fig. 4f) and corresponding EDX elemental mapping image (Fig. 4g) reveal that the Co, C, O and N elements have the same distribution profile, suggesting that the Co_3O_4/CN HNPs is sufficiently hybridized after an annealing treatment. As for as-synthesized Co_3O_4, its mainly exposed crystalline plane (Fig. 4h, i) and representative SAED patterns (Fig. S6) are consistent with above-mentioned Co_3O_4/CN HNPs. But its main nanoparticle size of 20–50 nm is much larger than that of Co_3O_4/CN HNPs, illustrating that the introduction of carbonaceous material has a decisive function in dispersing anchored Co_3O_4 nanoparticles, which echoes with the result of XRD above. Moreover, the EDS analysis as shown in Fig. S7 and Fig. S8, the mass fraction of Co element of as-synthesized Co_3O_4 is 70.35%., which is approximately equal to the corresponding ICP results (71.82%) in Table S2. On the other hand, the mass fraction of Co element of Co_3O_4/CN HNPs is 45.71% significantly higher than its 38.54% from ICP results in Table S2. These results conclude that when compared with the as-synthesized Co_3O_4, the Co ions are much more favorably exposed to the surface of Co_3O_4 in Co_3O_4/CN HNPs, which is beneficial to the increase of electrocatalytically active sites for OER.

The X-ray photoelectron spectroscopy (XPS) is employed to gain further insight into the composition and chemical states of Co_3O_4/CN HNPs, as-synthesized Co_3O_4, and PANI. As seen in Fig. 5a, the corresponding XPS survey spectra clearly demonstrate that the signals of C, N, Co and O appear in Co_3O_4/CN HNPs and the signals of Co and O appear in as-synthesized Co_3O_4, while the signals of C, N and O appear in PANI. The high-resolution XPS spectrum of Co 2p is shown in Fig. 5b, in which two core-level peaks situated at around 705.5 eV and 780.0 eV are attributed to $Co2p_{1/2}$ and $Co2p_{3/2}$, respectively. After deconvolution for $Co2p_{3/2}$, the peaks around at 779.2 and 780.9 correspond to the Co^{3+} $2p_{3/2}$ and Co^{2+} $2p_{3/2}$, respectively. The binding energy of Co $2p_{3/2}$ of Co_3O_4/CN HNPs exhibits a slightly negative shift, compared with the as-synthesized Co_3O_4, thus identifying the existence of interfacial

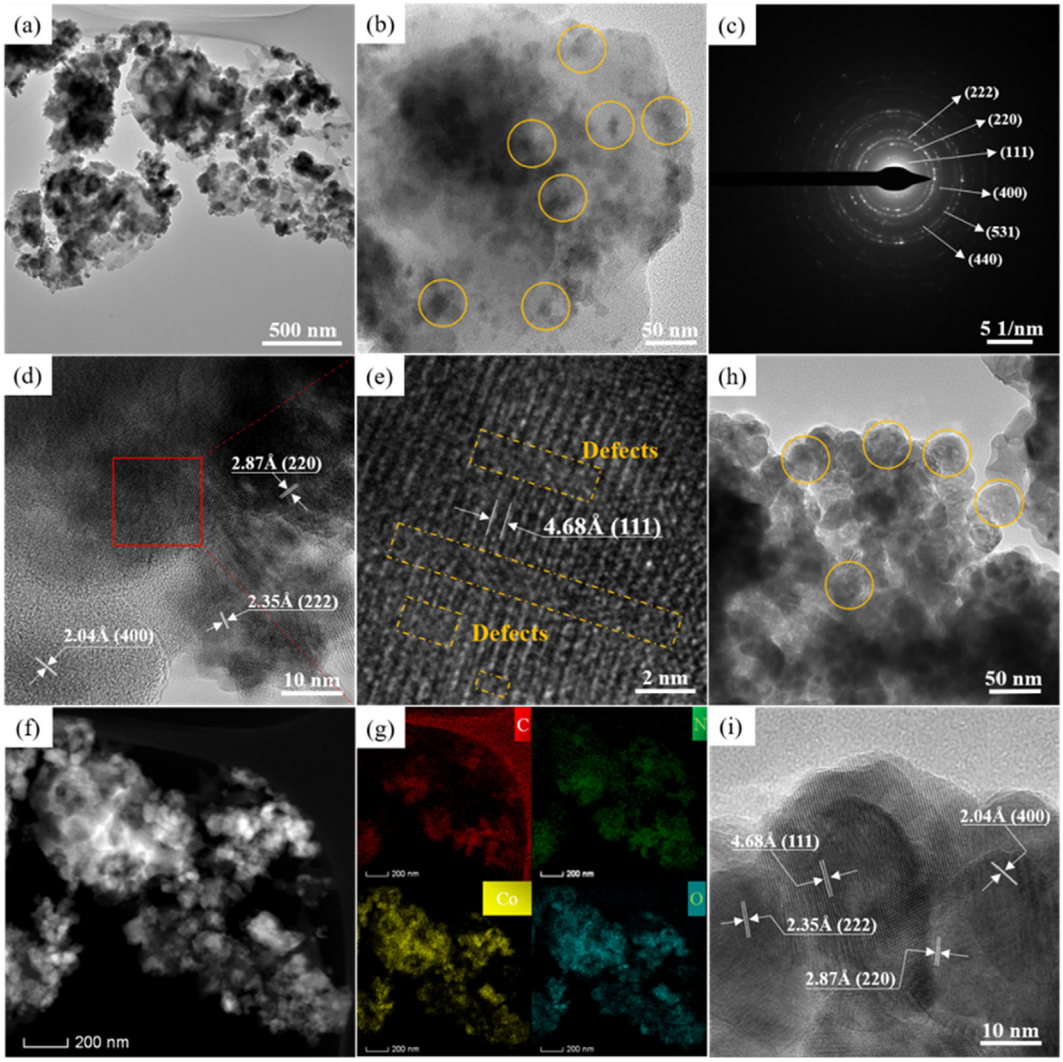

Fig. 4. (a) TEM image, (b) Magnified TEM image, (c) SAED pattern, (d, e) HRTEM images, (h) HADDF-STEM image and (g) EDS elemental mapping images of C, N, Co, O element of Co_3O_4/CN HNPs. (h) TEM image and (i) HRTEM image of as-synthesized Co_3O_4.

electron transfer from Co to N though Co—N coordinate bonds over the interfacial sites of Co_3O_4/CN HNPs [54,55]. In addition, the ratio of Co^{2+}/Co^{3+} of Co_3O_4/CN HNPs is calculated to be 0.87, much higher than that of the as-synthesized Co_3O_4 (0.42), indicating the existence of abundant Co^{2+} species over the Co_3O_4/CN HNPs, which can be served as the active sites for OER due to a favorability of formation of OOH* species over the Co^{2+} structures [56,57]. Besides, according to the electroneutrality principle, the increase of Co^{2+} species is indicative of the enhanced oxygen vacancies survived on the surface [58]. This result can be further confirmed by the high-resolution XPS spectrum of O 1s in Fig. 5c, which is divided into four main characteristic peaks (denoted as O1, O2, O3 and O4) [59]. Usually, the lowest energy peak at about 529.1–529.6 eV (O1) is indexed to metal-oxygen bond; The peak at 530.8 eV (O2) can be assigned to hydroxy species; The peak at 531.5–531.7 eV (O3) is associated with the surface oxygen vacancies species; The peak at 532.8 eV (O4) is assigned to the surface-adsorbed water molecules. Surprisingly, the O3 ratio (44.2%) of Co_3O_4/CN HNPs is much higher than that of as-synthesized Co_3O_4 (28.3%), confirming that there are more oxygen vacancies remaining over the Co_3O_4/CN HNPs [60]. It is noticeable that the electrons located on oxygen vacancies defects of Co_3O_4 are more favorable to excite to the conduction band, and thus enhance electronic conductivity for Co_3O_4-containing materials, which is of great significance and may contribute to improving electrocatalytic performance [47]. The high-resolution XPS spectrum of N 1s of Co_3O_4/CN HNPs as shown in Fig. 5d, in addition to the existence of peaks relative to pyridinic-N (398.5 eV), pyrrolic-N (400.2 eV), and graphitic-N (401.1 eV), a distinct peak situated at 399.4 eV can be attributed to the Co—N_x feature bonds, which is consistent with FTIR results, also further confirming the N elements are adequately doped into the Co_3O_4/CN HNPs as expected. Besides, the pyrrolic-N can function as metal-coordination sites due to their long-pair electrons while pyridinic-N is believed to approve for the releasing of O_2 molecules for reduction of OER overpotential [53,61]. Moreover, the N 1s XPS spectrum of PANI (Fig. 5d) contains four main peaks at 398.5 eV, 399.5 eV, 400.7 eV and 402.7 eV, which are attributed to the quionid imine (—N═), benzenoid imine (-NH-), positively charged imine (bipolaron state), and protonated amine (polaron state), respectively [62]. Noticeably, the N1s XPS peak of Co_3O_4/CN HNPs exhibits a slightly negative shift as compared with the PANI. This is because that the formation of Co—N coordinate bond of Co_3O_4/CN HNPs enables the electrons to transfer from Co to N over the interfacial sites between Co_3O_4.nanoparticles and C—N substrate, which corresponds to the increase of electron density in the N species and thus causes the lower binding energy of N1s XPS peak [47]. Furthermore, the C 1s XPS spectrum of Co_3O_4/CN HNPs is also investigated in detail, which can be divided into four characteristic peaks (Fig. S9a). The main peak at 284.2 eV corresponding to sp_2-carbon configuration, while the other peaks at 285.3 eV, 286.0 eV, and 288.3 eV are ascribed to C—N, C—O

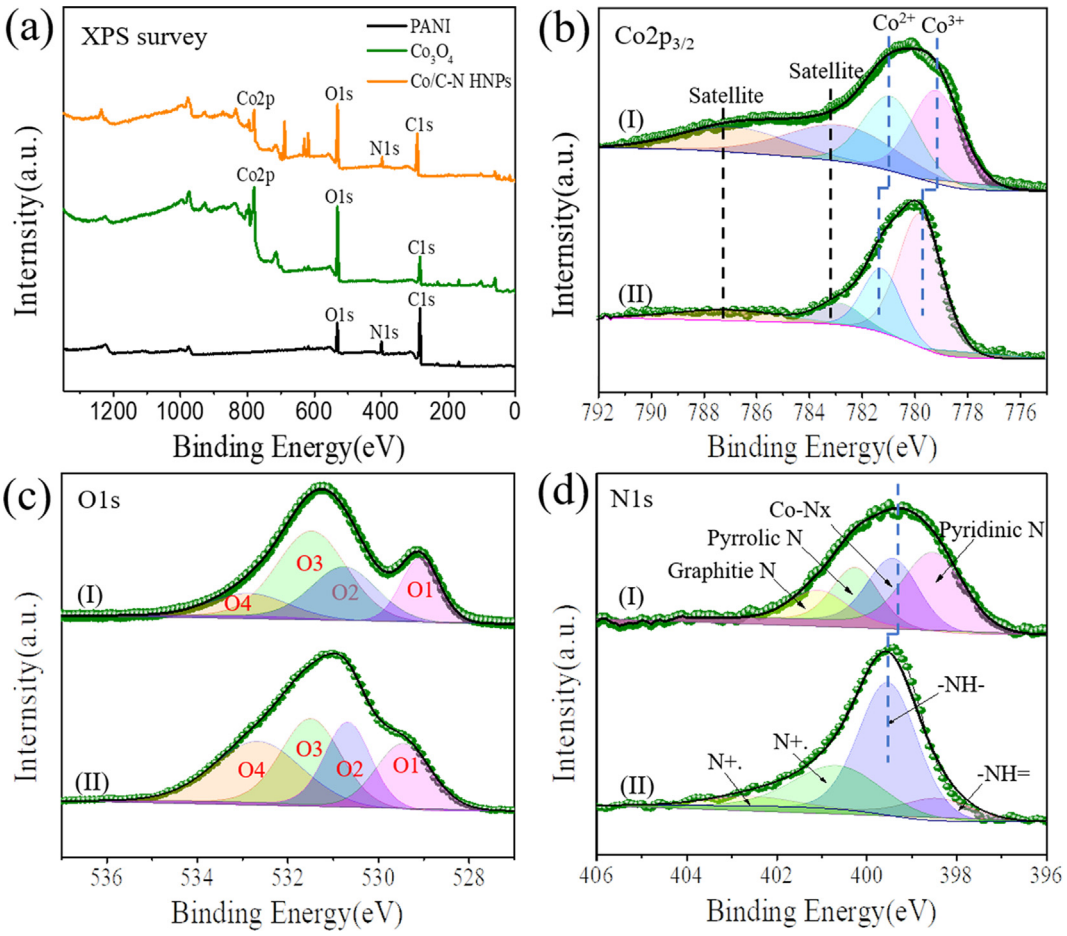

Fig. 5. (a) XPS survey. (b) $Co2p_{3/2}$, and (c) O1s of (I) Co_3O_4/CN HNPs and (II) as-synthesized Co_3O_4. (d) N 1s spectra of (I) Co_3O_4/CN HNPs and (II) PANI.

and O−C═O respectively [61], while the C1s XPS spectrum of PANI (Fig. S9b) can be deconvoluted into three peaks at the binding energy of 284.7 eV, 286.1 eV, and 288.4 eV, which are assigned to C═C/C−C, C−N and O−C═O, respectively [63]. Noticeably, there are no apparent negative or positive shifts of the C 1s XPS peak occurring by comparison between Co_3O_4/CN HNPs and PANI.

The electrocatalytic OER activity of Co_3O_4/CN HNPs is examined though the linear sweep voltammetry (LSV) curves that are recorded with *i*R correction in 1.0 M KOH solution using a three-electrode cell, whereas for comparison, Co_3O_4, PANI, and IrO_2 samples are also examined under the identical conditions. As illustrated in Fig. 6a, the polarization curve of Co_3O_4/CN HNPs presents a lower onset potential of 1.30 eV vs RHE than that of Co_3O_4 (1.44 eV), PANI (1.55 eV), and even IrO_2 (1.36 eV). Besides, the Co_3O_4/CN HNPs only needs an overpotential of 290 mV to attain a current density of 10 mA cm^{-2}, much lower than those of Co_3O_4 (397 mV), PANI (492 mV), and IrO_2 (346 mV), revealing a significantly promoted OER activity for Co_3O_4/CN HNPs. Impressively, this electrochemical performance can be comparable or even superior to more noticeable Co_3O_4-based OER electrocatalysts as recently reported (Table S1). Moreover, in order to explore OER kinetics, the Tafel plots are collected by their corresponding LSV curves. As expected, the Tafel plots of as-fabricated catalysts coincide well with the Tafel equation (Fig. 6b). The Tafel plots of Co_3O_4/CN HNPs is calculated to be 59 mV dec^{-1}, much smaller than those of Co_3O_4 (110 mV dec^{-1}), PANI (172 mV dec^{-1}), and IrO_2 (91 mV dec^{-1}), suggesting a favorable electrochemical OER kinetic occurring at Co_3O_4/CN HNPs electrode. Moreover, the electrochemical double layer capacitance (C_{dl}) of these three samples is conducted by monitoring CV scans in the non-Faradaic region as exhibited in Fig. S10a-c, which is proportional to electrochemically active surface areas (ESCAs) [64]. As shown in Fig. 6c, the calculated C_{dl} of Co_3O_4/CN HNPs, Co_3O_4, and PANI are 10.25, 7.34 and 6.78 mF cm^{-2}, respectively, illustrating that the Co_3O_4/CN HNPs has a larger ESCA for more exposed active sites available for OER.

To unveil the charge-transfer mechanism, the electrochemical impedance spectroscopy (EIS) are employed in the 1 M KOH electrolyte for above-mentioned electrocatalysts as shown in Fig. 6d. There are two distinct capacitance arcs that are displayed in the plot profile at the complicated plane in whole frequency domain. The first is regarding the mass transfer resistance from electrolyte to the exposed active sites in the high frequency, whereas the second is concerning charge transfer resistance and equivalent resistance of intermediates at the electrode/electrolyte interface in the low frequency [65]. The relaxation time of first semi-circle is much smaller than the second, revealing that either reaction charge transfer resistance or equivalent resistance of intermediates is predominant in the OER process. To get further insight into the kinetics of OER process, these all impedance results can be fitted with equivalent circuit of $R_s(C_{dl}R_{ct})(C_p(R_p(QR_q)))$ using both Z-view software and EIS Spectrum Analyzer program (Fig. 6e) [66–68]. Specifically, the R_s is the solution resistance; R_{dl} and C_{dl} are polarization resistance and capacitance of double layer, respectively; C_p is the double layer capacitance formed at the electrode/electrolyte interface; R_p is the reaction charge transfer resistance across the electrode/electrolyte interface. What's more, R_q and Q are equivalent resistance and psedo-capacitance that reflects the adsorption of intermediates at the working electrode, respectively. Consequently, it illustrates that the simulated EIS data presents (solid lines) a good match with the experimental ones (the scatters) (Fig. S11a–c) and the corresponding EIS fitting parameters are described in Table S3. It is noteworthy that the fitted R_q rather than R_p is relatively larger in the overall impedance,

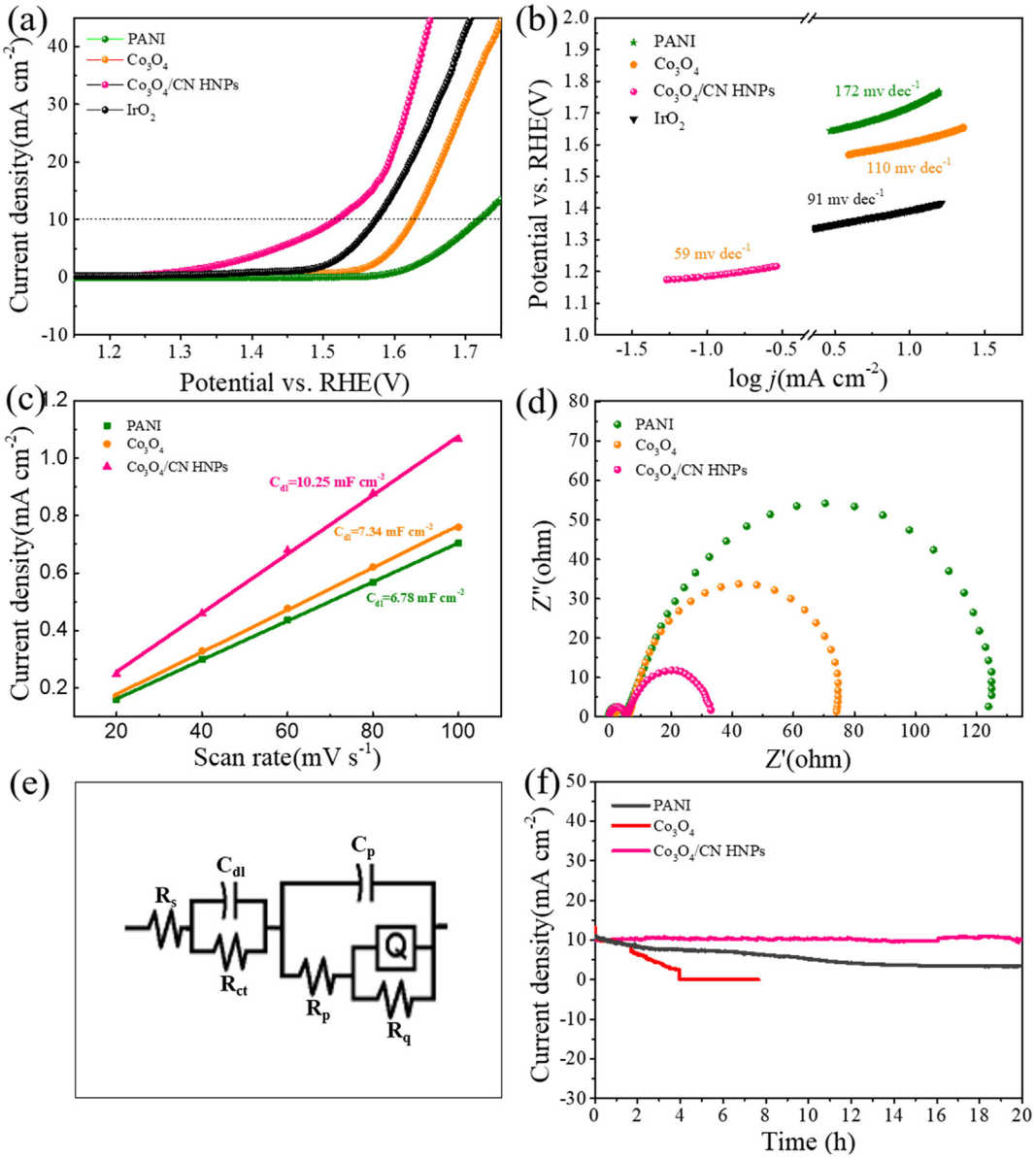

Fig. 6. (a) Polarization curves of PANI, as-synthesized Co_3O_4, Co_3O_4/CN HNPs and IrO_2 for OER at a scan rate of 10 mV s^{-1}. (b) The corresponding Tafel plots of PANI, as-synthesized Co_3O_4, Co_3O_4/CN HNPs and IrO_2. (c) The current density as a function of the scan rate for PANI, as-synthesized Co_3O_4 and Co_3O_4/CN HNPs. (d) EIS Nyquist plots of PANI, as-synthesized Co_3O_4 and Co_3O_4/CN HNPs at a constant potential of 1.52 V vs. RHE. (e) Simulated equivalent circuit simplified model of the as-obtained catalysts. (f) Time-dependent current density curves of the PANI, as-synthesized Co_3O_4 and Co_3O_4/CN HNPs with the set potential of 492 mV, 397 mV and 290 mV, respectively.

suggesting OER kinetics is mainly determined by the equivalent resistance about adsorption of intermediates for these three electrocatalysts. In this regard, the Co_3O_4/CN HNPs presents a much lower equivalent resistance of adsorbed intermediates when compared with those of as-synthesized Co_3O_4 and PANI, meaning its favorable formation of intermediates and rapid change transfer kinetics for OER. Considering the electrochemical stability of Co_3O_4/CN HNPs, we observe no obvious depletion in the current density during continuous operation for 20 h, whereas for PANI and especially as-synthesized Co_3O_4, it is the opposite. It is also detected that there are no changes about exposed lattice plane of Co_3O_4 nanoparticle in TEM images and corresponding SAED of Co_3O_4/CN HNPs after 20 h electrochemical stability measurement (Fig. S12 and Fig. S13). This is, the remarkable structural stability of Co_3O_4/CN HNPs caused by the strong interaction is suitable for its durability in OER. In addition, the Co_3O_4 is still observed from XRD pattern of Co_3O_4/CN HNPs after 20 h electrochemical measurement (Fig. S14), which can be regarded as the stable species for OER in alkaline environment.

4. Conclusions

In summary, an integrated defect-induced Co_3O_4/CN HNPs electrocatalyst is successfully synthesized via facile wetness-impregnation treatment followed by a thermal annealing. In this regard, the generated microcrystalline graphite structure of Co_3O_4/CN HNPs is propitious to the improvement of electrical conductivity for OER. It is also demonstrated that the pyrrolic-N species with long-pair electrons can function as metal-coordination sites, which can cause the formation of Co—N coordination bonds through the strong interaction of Co_3O_4 and C—N substrate, therefore, the structural stability of Co_3O_4/CN HNPs gets to be effectively strengthened and thus contributes to lower immigration probability of Co_3O_4 nanoparticles. Besides, the pyridinic-N species of Co_3O_4/CN HNPs is beneficial for releasing of O_2 molecules and reducing OER overpotential. More importantly, there are a number

of crystal defects and oxygen-vacancy defects existing in the Co_3O_4/CN HNPs, which help to improve the exposure of the active sites, facilitate electronic transfer, and optimize the adsorption energy for intermediates, thus enabling the extraordinary activities in catalyzing OER. In view of these reasons, Co_3O_4/CN HNPs gets a low overpotential of 290 mV at a current density of 10 mA cm^{-2} and a small Tafel slope of 59 mV dec^{-1} in 1 M KOH electrolyte, superior than those of Co_3O_4, PANI, and commercial IrO_2. The Co_3O_4/CN HNPs also exhibits good stability at a current density of 10 mA cm^{-2} for 20 h.

CRediT authorship contribution statement

Xiaodong Chen: Conceptualization, Methodology, Software, Investigation, Writing - original draft. **Ya Chen:** Validation, Formal analysis, Visualization, Software, Writing - original draft. **Xiang Luo:** Validation, Formal analysis, Visualization, Writing - original draft. **Hele Guo:** Conceptualization, Formal analysis. **Nannan Wang:** Visualization, Software. **Dawei Su:** Visualization, Software. **Chao Zhang:** Resources, Writing - review & editing, Supervision, Data curation. **Tianxi Liu:** Writing - review & editing. **Guoxiu Wang:** Resources, Writing - review & editing, Supervision, Data curation. **Lifeng Cui:** Resources, Writing - review & editing, Supervision, Data curation.

Declaration of Competing Interest

The authors declare that they have no known competing financial interests or personal relationships that could have appeared to influence the work reported in this paper.

Acknowledgements

This project is financially supported by the Startup Research Fund of Dongguan University of Technology (KCYKYQD2017015), the Postdoctoral Startup Research Fund of Dongguan University of Technology (196100040019), Leading Talents of Innovation and Entrepreneurship of the Dongguan City D2017(16)., and the Australian Research Council (ARC) through the ARC Discovery project (DP160104340).

Appendix A. Supplementary material

Supplementary data to this article can be found online at https://doi.org/10.1016/j.apsusc.2020.146626.

References

[1] J. Wang, W. Cui, Q. Liu, Z. Xing, A.M. Asiri, X. Sun, Recent progress in cobalt-based heterogeneous catalysts for electrochemical water splitting, Adv. Mater. 28 (2016) 215–230.
[2] V. Artero, M. Chavarot-Kerlidou, M. Fontecave, Splitting water with cobalt, Angew. Chem. Int. Ed. 50 (2011) 7238–7266.
[3] W. Zhang, W. Lai, R. Cao, Energy-related small molecule activation reactions: oxygen reduction and hydrogen and oxygen evolution reactions catalyzed by porphyrin- and corrole-based systems, Chem. Rev. 117 (2017) 3717–3797.
[4] B.M. Hunter, H.B. Gray, A.M. Muller, Earth-abundant heterogeneous water oxidation catalysts, Chem. Rev. 116 (2016) 14120–14136.
[5] Q. Zhao, Z. Yan, C. Chen, J. Chen, Spinels: Controlled preparation, oxygen reduction/evolution reaction application, and beyond, Chem. Rev. 117 (2017) 10121–10211.
[6] T. Reier, H.N. Nong, D. Teschner, R. Schlögl, P. Strasser, Electrocatalytic oxygen evolution reaction in acidic environments - reaction mechanisms and catalysts, Adv. Energy Mater. 7 (2017) 1601275.
[7] Y.P. Zhu, C. Guo, Y. Zheng, S.Z. Qiao, Surface and interface engineering of noble-metal-free electrocatalysts for efficient energy conversion processes, Acc. Chem. Res. 50 (2017) 915–923.
[8] F. Song, L. Bai, A. Moysiadou, S. Lee, C. Hu, L. Liardet, X. Hu, Transition metal oxides as electrocatalysts for the oxygen evolution reaction in alkaline solutions: an application-inspired renaissance, J. Am. Chem. Soc. 140 (2018) 7748–7759.
[9] B. You, Y. Sun, Innovative strategies for electrocatalytic water splitting, Acc. Chem. Res. 51 (2018) 1571–1580.
[10] C. Tang, H.F. Wang, X.L. Zhu, B.Q. Li, Q. Zhang, Advances in hybrid electrocatalysts for oxygen evolution reactions: rational integration of NiFe layered double hydroxides and nanocarbon, Part. Part. Syst. Charact. 33 (2016) 473–486.
[11] P. Strasser, Free Electrons to Molecular Bonds and Back: closing the energetic oxygen reduction (ORR)-oxygen evolution (OER) cycle using core-shell nanoelectrocatalysts, Acc. Chem. Res. 49 (2016) 2658–2668.
[12] Y. Guo, T. Park, J.W. Yi, J. Henzie, J. Kim, Z. Wang, B. Jiang, Y. Bando, Y. Sugahara, J. Tang, Y. Yamauchi, Nanoarchitectonics for transition-metal-sulfide-based electrocatalysts for water splitting, Adv. Mater. 31 (2019) e1807134.
[13] K. Zhu, X. Zhu, W. Yang, Application of in situ techniques for the characterization of NiFe-based oxygen evolution reaction (OER) electrocatalysts, Angew. Chem. Int. Ed. 58 (2019) 1252–1265.
[14] J. Shen, J. Gao, L. Ji, X. Chen, C. Wu, Three-dimensional interlinked Co_3O_4-CNTs hybrids as novel oxygen electrocatalyst, Appl. Surf. Sci. 497 (2019) 143818.
[15] Y. Tian, L. Cao, P. Qin, Bimetal－organic framework derived high-valence-state Cu-doped Co_3O_4 porous nanosheet arrays for efficient oxygen evolution and water splitting, ChemCatChem 11 (2019) 4420–4426.
[16] L. Zhang, H. Li, K. Li, L. Li, J. Wei, L. Feng, Q. Fu, Morphology-controlled fabrication of Co_3O_4 nanostructures and their comparative catalytic activity for oxygen evolution reaction, J. Alloys Compd. 680 (2016) 146–154.
[17] X. Zhou, X. Shen, Z. Xia, Z. Zhang, J. Li, Y. Ma, Y. Qu, Hollow fluffy Co_3O_4 cages as efficient electroactive materials for supercapacitors and oxygen evolution reaction, ACS Appl. Mater. Interfaces 7 (2015) 20322–20331.
[18] H. Wang, T. Zhou, D. Li, H. Gao, G. Gao, A. Du, H. Liu, Z. Guo, Ultrathin cobaltosic oxide nanosheets as an effective sulfur encapsulation matrix with strong affinity toward polysulfides, ACS Appl. Mater. Interfaces 9 (2017) 4320–4325.
[19] L. Xu, Q. Jiang, Z. Xiao, X. Li, J. Huo, S. Wang, L. Dai, Plasma-engraved Co_3O_4 nanosheets with oxygen vacancies and high surface area for the oxygen evolution reaction, Angew. Chem. Int. Ed. 55 (2016) 5277–5281.
[20] Z. Wu, L.P. Sun, M. Yang, L.H. Huo, H. Zhao, J.C. Grenier, Facile synthesis and excellent electrochemical performance of reduced graphene oxide-Co_3O_4 yolk-shell nanocages as a catalyst for oxygen evolution reaction, J. Mater. Chem. A 4 (2016) 13534–13542.
[21] Y.J. Wang, H.B. Fan, A. Ignaszak, L. Zhang, S.Q. Shao, D.P. Wilkinson, J.J. Zhang, Compositing doped-carbon with metals, non-metals, metal oxides, metal nitrides and other matierials to form bifunctinal electrocatalysts to enhance metal-air battery oxygen reductin and evolution reactions, Chem. Eng. J. 348 (2018) 416–437.
[22] M.J. Chen, L. Wang, H.P. Yang, S. Zhao, H. Xu, G. Wu, Nanocarbon/oxide composite catalysts for bifunctional oxygen reduction and evolution in reversible alkaine fuel cells: a mini review, J. Power Sources 375 (2018) 277–290.
[23] W. Zhang, K. Zhou, Ultrathin two-dimensional nanostructured materials for highly efficient water oxidation, Small 13 (2017) 1700806.
[24] M. Tahir, L. Pan, F. Idrees, X.W. Zhang, L. Wang, J.J. Zhou, Z.L. Wang, Electrocatalytic oxygen evolution reaction for energy conversion and storage: a comprehensive review, Nano Energy 37 (2017) 136–157.
[25] H. Osgood, S.V. Devaguptapu, H. Xu, J. Cho, G. Wu, Transition metal (Fe Co, Ni, and Mn) oxides for oxygen reduction and evulutiong bifunctional catalysts in alkaine media, Nano Today 11 (2016) 601–625.
[26] M. Hamdani, R.N. Singh, P. Chartier, Co_3O_4 and co-based spinel oxides bifunctional oxygen electrodes, Int. J. Electrochem. Sci. 5 (2010) 556–577.
[27] J.F. Xie, H. Zhang, S. Li, R.X. Wang, X. Su, M. Zhou, J.F. Zhou, X.W. Lou, Y. Xie, Defect-rich MoS_2 ultrathin nanosheets with additional active edge sites for enhanced electrocatalytic hydrogen evolution, Adv. Mater. 25 (2013) 5807–5813.
[28] C.Y. Guo, X.J. Liu, L.F. Guo, X.J. Ma, M.Z. Zhao, J.Z. Zhou, X. Kuang, W.Q. Deng, X. Sun, Q. Wei, Oxygen defect engineering in cobalt iron oxide nanosheets for promoted overall water splitting, J. Mater. Chem. A 7 (2019) 21704–21710.
[29] X. Li, X. Su, Y. Pei, J. Liu, X. Zheng, K. Tang, G. Guan, X. Hao, Generation of edge dislocation defects in Co_3O_4 catalysts: an efficient tactic to improve catalytic activity for oxygen evolution, J. Mater. Chem. A 7 (2019) 10745–10750.
[30] Y. Yin, J.C. Han, Y.M. Zhang, X.H. Zhang, P. Xu, Q. Yuan, L. Samad, X.J. Wang, Y. Wang, Z.H. Zhang, P. Zhang, X.Z. Cao, B. Song, S. Jin, Contributions of phase, sulfur vacancies, and edges to the hydrogen evolution reaction catalytic activity of porous molybdenum disulfide nanosheets, J. Am. Chem. Soc. 138 (2016) 7965–7972.
[31] C.L. Hu, L. Zhang, Z.J. Zhao, A. Li, X.X. Chang, J.L. Gong, Synergism of geometric construction and electronic regulation: 3D Se-$(NiCo)_{S-x}/(OH)_{(x)}$ nanosheets for highly efficient overall water splitting, Adv. Mater. 30 (2018) 1705538.
[32] X.J. Fan, Y.Y. Liu, S. Chen, J.J. Shi, J.J. Wang, A.L. Fan, W.Y. Zan, S.D. Li, W.A. Goddard, X.M. Zhang, Defect-enriched iron fluoride-oxide nanoporous thin films bifunctional catalyst for water splitting, Nat. Commun. 9 (2018) 1809.
[33] R. Gao, Z. Li, X. Zhang, J. Zhang, Z. Hu, X. Liu, Carbon-dotted defective CoO with oxygen vacancies: a synergetic design of bifunctional cathode catalyst for Li–O_2 batteries, ACS Catal. 6 (2015) 400–406.
[34] R. Zhang, Y.C. Zhang, L. Pan, G.Q. Shen, N. Mahmood, Y.H. Ma, Y. Shi, W. Jia, L. Wang, X. Zhang, W. Xu, J.J. Zou, Engineering cobalt defects in cobalt oxide for highly efficient electrocatalytic oxygen evolution, ACS Catal. 8 (2018) 3803–3811.
[35] S. Chen, Z. Wei, X. Qi, L. Dong, Y.G. Guo, L. Wan, Z. Shao, L. Li, Nanostructured polyaniline-decorated Pt/C@PANI core-shell catalyst with enhanced durability and activity, J. Am. Chem. Soc. 134 (2012) 13252–13255.
[36] J.X. Feng, L.X. Ding, S.H. Ye, X.J. He, H. Xu, Y.X. Tong, G.R. Li, $Co(OH)_2$ @PANI hybrid nanosheets with 3D networks as high-performance electrocatalysts for hydrogen evolution reaction, Adv. Mater. 27 (2015) 7051–7057.
[37] Y.T. Dong, J.X. Feng, G.R. Li, Transition metal ion-induced high electrocatalytic performance of conducting polymer for oxygen and hydrogen evolution reactions, Chem. Phys. 218 (2017) 1700359.
[38] C. Wang, Z. Li, L. Wang, X. Lu, S. Wang, X. Niu, Vertical-space-limit synthesis of bifunctional Fe, N-Co doped 2D multilayer graphene electrocatalysts for Zn-Air

battery, Energy Technol.-Ger. 7 (2019) 1900123.
[39] K. Sarkar, A. Debnath, K. Deb, A. Bera, B. Saha, Effect of NiO incorporation in charge transport of polyaniline: improved polymer based thermoelectric generator, Energy 177 (2019) 203–210.
[40] P.F. Liu, L. Zhang, L.R. Zheng, H.G. Yang, Surface engineering of nickel selenide for an enhanced intrinsic overall water splitting ability, Mater. Chem. Front. 2 (2018) 1725–1731.
[41] S. Wang, F. Liu, C. Gao, T. Wan, L. Wang, L. Wang, L. Wang, Enhancement of the thermoelectric property of nanostructured polyaniline/carbon nanotube composites by introducing pyrrole unit onto polyaniline backbone via a sustainable method, Chem. Eng. J. 370 (2019) 322–329.
[42] A. Jevremović, P. Bober, M. Mičušík, J. Kuliček, U. Acharya, J. Pfleger, M. Milojević-Rakić, D. Krajišnik, M. Trchová, J. Stejskal, G. Ćirić-Marjanović, Synthesis and characterization of polyaniline/BEA zeolite composites and their application in nicosulfuron adsorption, Micropor. Mesopor. Mat. 287 (2019) 234–245.
[43] M. Singh, A. Sahu, S. Mahata, P. Shukla, A. Rai, V.K. Rai, Efficient electrocatalytic oxidation of p-phenylenediamine using a novel PANI/ZnO anchored bio-reduced graphene oxide nanocomposite, New J. Chem. 43 (2019) 6500–6506.
[44] V. Venkatachalam, A. Alsalme, A. Alswieleh, R. Jayavel, Shape controlled synthesis of rod-like Co_3O_4 nanostructures as high-performance electrodes for supercapacitor applications, J. Mater. Sci.-Mater. El. 29 (2018) 6059–6067.
[45] C.W. Tang, C.B. Wang, S.H. Chien, Characterization of cobalt oxides studied by FT-IR Raman, TPR and TG-MS, Thermochimica Acta. 473 (2008) 68–73.
[46] X. Wang, H.Y. Chen, W.M.H. Sachtler, Mechanism of the Selective Reduction of NOx over Co/MFI: Comparison with Fe/MFI, J. Catal. 197 (2001) 281–291.
[47] Z. Wang, W. Xu, X. Chen, Y. Peng, Y. Song, C. Lv, H. Liu, J. Sun, D. Yuan, X. Li, X. Guo, D. Yang, L. Zhang, Defect-rich nitrogen doped Co_3O_4/C porous nanocubes enable high-efficiency bifunctional oxygen electrocatalysis, Adv. Funct. Mater. 29 (2019) 1902875.
[48] H.Q. Chu, D. Zhang, B.W. Jin, M. Yang, Impact of morphology on the oxygen evolution reaction of 3D hollow Cobalt-Molybdenum Nitride, Appl. Catal. B-Environ. 255 (2019) 117744.
[49] J. Hou, Z. Liu, P. Zhang, A new method for fabrication of graphene/polyaniline nanocomplex modified microbial fuel cell anodes, J. Power Sources 224 (2013) 139–144.
[50] D.A.L. Almeida, A.B. Couto, N.G. Ferreira, Flexible polyaniline/reduced graphene oxide/carbon fiber composites applied as electrodes for supercapacitors, J. Alloys Compd. 788 (2019) 453–460.
[51] X. Zhu, Z. Ni, L. Dong, Z. Yang, L. Cheng, X. Zhou, Y. Xing, J. Wen, M. Chen, In-situ modulation of interactions between polyaniline and graphene oxide films to develop waterborne epoxy anticorrosion coatings, Prog. Org. Coat. 133 (2019) 106–116.
[52] P. Tan, Z. Wu, B. Chen, H. Xu, W. Cai, M. Ni, Exploring oxygen electrocatalytic activity and pseudocapacitive behavior of Co_3O_4 nanoplates in alkaline solutions, Electrochim. Acta 310 (2019) 86–95.
[53] Y. Ha, L. Shi, Z. Chen, R. Wu, Phase-transited lysozyme-driven formation of self-supported Co_3O_4@C nanomeshes for overall water splitting, Adv. Sci. 6 (2019) 1900272.
[54] M. Yang, W. Lu, R. Jin, X.C. Liu, S. Song, Y. Xing, Superior oxygen evolution reaction performance of $Co_3O_4/NiCo_2O_4$/Ni foam composite with hierarchical structure, ACS Sustain. Chem. Eng. 7 (2019) 12214–12221.
[55] A. Muthurasu, V. Maruthapandian, H.Y. Kim, Metal-organic framework derived Co_3O_4/MoS_2 heterostructure for efficient bifunctional electrocatalysts for oxygen evolution reaction and hydrogen evolution reaction, Appl. Catal. B-Environ. 248 (2019) 202–210.
[56] M. Li, F. Luo, Q. Zhang, Z.H. Yang, Z.K. Xu, Atomic layer Co_3O_{4-x} nanosheets as efficient and stable electrocatalyst for rechargeable zinc-air batteries, J. Catal. 381 (2020) 395–401.
[57] Y. Xu, F.C. Zhang, T. Sheng, T. Ye, D. Yi, Y.J. Yang, S.J. Liu, X. Wang, J.N. Yao, Clarifying the controversial catalytic active sites of Co_3O_4 for the oxygen evolution reaction, J. Mater. Chem. A 7 (2019) 23191–23198.
[58] B. Qiu, C. Wang, N. Zhang, L. Cai, Y. Xiong, Y. Chai, CeO_2-Induced Interfacial Co^{2+} octahedral sites and oxygen vacancies for water oxidation, ACS Catal. 9 (2019) 6484–6490.
[59] R. Li, Y. Guo, H. Chen, K. Wang, R. Tan, B. Long, Y. Tong, P. Tsiakaras, S. Song, Y. Wang, Anion–cation double doped Co_3O_4 microtube architecture to promote high-valence Co species formation for enhanced oxygen evolution reaction, ACS Sustain. Chem. Eng. 7 (2019) 901–11910.
[60] Y. Liu, C. Ma, Q. Zhang, W. Wang, P. Pan, L. Gu, D. Xu, J. Bao, Z. Dai, 2D electron gas and oxygen vacancy induced high oxygen evolution performances for advanced Co_3O_4/CeO_2 nanohybrids, Adv. Mater. 31 (2019) e1900062.
[61] Y. Li, C. Zhong, J. Liu, X. Zeng, S. Qu, X. Han, Y. Deng, W. Hu, J. Lu, Atomically thin mesoporous Co_3O_4 layers strongly coupled with N-rGO nanosheets as high-performance bifunctional catalysts for 1D knittable zinc-air batteries, Adv. Mater. 30 (2018) 1703657.
[62] G.M.O. Barra, M.E. Leyva, M.M. Gorelova, B.G. Soares, S. Marcio, X-ray photoelectron spectroscopy and electrical conductivity of polyaniline doped with dodecylbenzenesulfonic acid as a function of the synthetic method, Appl. Organ. Chem. 5 (1991) 203–206.
[63] S. Biniak, G. Zymanski, J. Siedlewski, A. Swiatkowski, The characterization of activated carbons with oxygen and nitrogen surface groups, Carbon 35 (1997) 1799–1810.
[64] B. Zhu, G. Yang, D. Gao, Y. Wu, J. Zhao, Y. Fu, S. Ma, Special atmosphere annealed Co_3O_4 porous nanoclusters with oxygen defects and high proportion of Co^{2+} for oxygen evolution reaction, J. Alloys Compd. 806 (2019) 163–169.
[65] E.M. Garcia, H.A. Tarôco, T. Matencio, R.Z. Domingues, J.A.F. dos Santos, Electrochemical study of $La_{0.6}Sr_{0.4}Co_{0.8}Fe_{0.2}O_3$ during oxygen evolution reaction, Int. J. Hydrogen Energ. 37 (2012) 6400–6406.
[66] Z. Zhang, D. Zhou, J. Liao, X. Bao, H. Yu, Synthesis of high crystalline nickel-iron hydrotalcite-like compound as an efficient electrocatalyst for oxygen evolution reaction, Int. J. Energ. Res. 43 (2019) 1460–1467.
[67] A. Alobaid, C. Wang, R.A. Adomaitis, mechanism and kinetics of HER and OER on NiFe LDH films in an alkaline electrolyte, J. Electrochem. Soc. 165 (2018) J3395–J3404.
[68] Y. Lai, Y. Li, L. Jiang, W. Xu, X. Lv, J. Li, Y. Liu, Electrochemical behaviors of co-deposited Pb/Pb–MnO_2 composite anode in sulfuric acid solution – Tafel and EIS investigations, J. Electroanal. Chem. 671 (2012) 16–23.